

1 **GPU-accelerated 3-D viscoacoustic wave equation**
2 **modeling with natural-attenuation absorbing boundary**
3 **conditions**

4 **Bei Li¹, Yunyue Elita Li¹, and Arthur Cheng¹**

5 ¹Department of Civil and Environmental Engineering, National University of Singapore, 117576 Singapore

6 **Key Points:**

- 7 • We propose new natural-attenuation absorbing boundary conditions to improve
8 modeling efficiency of viscoacoustic wave equation.
- 9 • We simplify the time-stepping error compensators for two-step extrapolation in
10 viscoacoustic wave equation modeling with decoupled fractional Laplacians (DFLs).
- 11 • We provide an open-source python package for GPU-accelerated 3-D DFL visco-
12 coustic wave equation modeling.

Corresponding author: Yunyue Elita Li, elita.li@nus.edu.sg

13 **Abstract**

14 Viscoacoustic wave equation with decoupled fractional Laplacians (DFLs) describes P-
 15 wave propagation through the anelastic earth under the assumption of frequency-independent
 16 Q . Numerical solutions of this equation often employ 2nd-order finite differences for the
 17 time derivatives and spectral methods for the spatial DFLs. The spectral methods re-
 18 quire multiple Fourier transforms at each time step, leading to large computational cost
 19 especially in 3-D case. To accelerate the viscoacoustic wave simulation, GPU-based com-
 20 putation is preferred. We propose new absorbing boundary conditions (ABCs) for GPU-
 21 accelerated viscoacoustic wave equation modeling. The new ABCs naturally attenuate
 22 the outgoing waves by padding the original velocity and Q models with optimized ab-
 23 sorbing layers. In comparison with the conventional ABCs, the natural-attenuation ABCs
 24 (naABCs) require no special treatment for the absorbing layers, thus provide around 2x
 25 speedup for the GPU-based time marching process. We also simplify the 2nd-order k -
 26 space compensators for the time-stepping error introduced by the 2nd-order temporal
 27 FDs. Considering simple and convenient implementations of GPU acceleration in python,
 28 we develop a python package for 3-D DFL viscoacoustic wave equation modeling with
 29 the application of naABCs and simplified time-stepping error compensators. The mod-
 30 eling examples not only validate the feasibility of our package in simulating the viscoa-
 31 coustic wave propagation, but also demonstrate the satisfying absorbing effect and ad-
 32 vantageous efficiency of the naABCs.

33 **Plain Language Summary**

34 Accurately and efficiently modeling the wave propagation through the anelastic earth
 35 is a key procedure when investigating the underground situations using seismic waves.
 36 Simulating the compressional wave propagation in lossy media requires solving the vis-
 37 coacoustic wave equation, where GPU parallelization can significantly improve the ef-
 38 ficiency. We proposed new natural-attenuation absorbing boundary conditions (naABCs),
 39 which show superior efficiency in the GPU-accelerated viscoacoustic wave equation mod-
 40 eling. Based on the naABCs, we developed a python package for GPU-accelerated 3-D
 41 viscoacoustic wave equation modeling. This package provides viscoacoustic wave sim-
 42 ulations in 3-D with balanced accuracy and efficiency.

43 **1 Introduction**

44 Seismic waves experience attenuation when propagating through real earth due to
 45 underground anelasticity. High seismic attenuation, quantified by low quality factor Q ,
 46 often associates with gas accumulation (Zhu et al., 2017) or magma bodies (Sanders et
 47 al., 1995). The attenuated seismic waveforms exhibit both amplitude decay and phase
 48 distortion, which requires Q compensation when building underground elastic models
 49 from seismic data space (Zhang et al., 2013; Dutta & Schuster, 2014). Since the atten-
 50 uation is considered to be almost linear with frequency, Q is reasonably assumed con-
 51 stant in many frequency bands (McDonald et al., 1958). Based on the precise constant-
 52 Q model (Kjartansson, 1979), Zhu and Harris (2014) developed a viscoacoustic wave equa-
 53 tion with decouple fractional Laplacians (DFLs). This equation avoids saving the wave-
 54 field history required by conventional constant- Q wave equation with fractional time deriva-
 55 tive (Carcione et al., 2002). More importantly, due to separated terms representing am-
 56 plitude decay and phase distortion, this wave equation accomplishes accurate adjoint prop-
 57 agation with attenuation compensation by simply reversing the sign of the amplitude-
 58 decay term. Therefore, implementation with DFLs has been widely applied in Q -compensated
 59 reverse time migration (RTM) (Zhu et al., 2014), least-squares RTM (LSRTM) (Sun et
 60 al., 2016), and full waveform inversion (FWI) (Xue et al., 2018).

61 Despite its popularity, DFL viscoacoustic wave equation is difficult to solve due to
 62 the spatially varying power of DFLs in a heterogeneous Q model. Zhu et al. (2014) achieved

63 spatially constant power by averaging the heterogeneous Q so that simple pseudospectral
 64 method can be applied. Such implementation compromises the modeling accuracy
 65 and stability, especially when large Q contrasts exist. Chen et al. (2016) also achieved
 66 spatially constant power with an extra Laplacian term based on Taylor expansion. It pro-
 67 vides better approximation than the averaging strategy, but a single optimal power still
 68 shows accuracy deterioration for low Q values. Yao et al. (2017) proposed local solvers
 69 for DFLs using Hermite distributed approximating functional method. However, due to
 70 large rectangular stencils, the computational cost is not reduced in comparison with spec-
 71 tral methods. To achieve a flexible balance between the accuracy and efficiency, low-rank
 72 approximation (Fomel et al., 2013) is adapted for solving DFL viscoacoustic wave equa-
 73 tion. Chen et al. (2014) proposed the two-step extrapolation scheme, where DFLs are
 74 approximated using low-rank decomposition, while time derivatives are approximated
 75 using 2nd-order FDs. With superior temporal accuracy and stability, Sun et al. (2016)
 76 proposed the one-step extrapolation scheme, which utilizes low-rank decomposition to
 77 directly approximate the phase of the complex analytic wavefield. Chen et al. (2019) and
 78 N. Wang et al. (2020) developed 1st and 2nd-order k -space compensators for time-stepping
 79 errors in the two-step extrapolation, leading to improved temporal accuracy and stabil-
 80 ity while still marching the real wavefield along time. Although these compensators hardly
 81 influence the computational cost for the time marching process, they do increase the com-
 82 putational complexity of the mixed-domain operators for low-rank decomposition. Here,
 83 we simplify the 2nd-order k -space compensators (N. Wang et al., 2020) for more efficient
 84 low-rank decomposition with barely compromised accuracy and stability. At each time
 85 step, multiple forward and inverse FFTs on the wavefield snapshots are necessary, re-
 86 sulting in enormous computational cost in 3-D modeling scenarios. Therefore, GPU ac-
 87 celeration has been utilized to provide acceptable efficiency for viscoacoustic wave sim-
 88 ulation (N. Wang et al., 2020) and its application in Q -compensated RTM (Y. Wang et
 89 al., 2019).

90 To properly simulate the wave propagation in the earth whose dimensions are much
 91 larger than the computational domain, absorbing boundary conditions (ABCs) are nec-
 92 essary to suppress the wraparound effects in the bounded modeling area. Commonly used
 93 ABCs, such as Perfectly Matched Layers (PMLs) (Berenger et al., 1994) and hybrid ABCs
 94 (hABCs) (Liu & Sen, 2010), have been applied in viscoacoustic wave equation model-
 95 ing (Ren & Liu, 2013; Chen et al., 2019). These conventional ABCs involve special treat-
 96 ments for the absorbing layers at each time step, e.g., updating one-way-wave-equation
 97 (OWWE) for hABCs, or calculating extra convolutional terms for convolutional PMLs,
 98 therefore, impede the modeling efficiency. Due to smaller memory, GPU implemen-
 99 tations of such boundary conditions slow down more significantly compared to CPU im-
 100 plementations. We propose the natural-attenuation ABCs (naABCs), which extend the
 101 velocity and Q models with optimized absorbing layers, so that the outgoing waves will
 102 attenuate naturally without any special treatments during the time marching process.
 103 The optimization for the minimum absorbing-layer number and corresponding model pa-
 104 rameters (velocity and Q) at each layer, is established upon three constraints: (1) pre-
 105 determined tolerance for the boundary artifacts (artificial reflections and wraparounds)
 106 amplitude, (2) Nyquist wavenumber, and (3) stability condition. We develop an efficient
 107 algorithm to solve this optimization and provide padding strategy for heterogeneous me-
 108 dia. Since applying naABCs is simply extending the original velocity and Q models be-
 109 fore the time-marching process, they are readily applicable to any other numerical schemes
 110 for constant- Q viscoacoustic wave equation modeling either in the time or frequency do-
 111 main, such as global finite-differences (Xu et al., 2018) and the one-step extrapolation
 112 scheme (Sun et al., 2016).

113 Utilizing the naABCs and the two-step extrapolation with time-stepping error com-
 114 pensation, we develop a python package for GPU-accelerated 3-D DFL viscoacoustic wave
 115 equation modeling. This open-source modeling package, as the major contribution of this

paper, features a great balance between accuracy and efficiency, achieved by innovations in the simplified time-stepping error compensation and the proposed naABCs.

We organize this article as follows: first, we introduce the DFL viscoacoustic wave equation and its two-step extrapolation scheme with the simplified time-stepping error compensation; next, we propose the new naABCs and provide two analytical tests; finally, we use two modeling examples to demonstrate the satisfying absorbing effect and superior modeling efficiency.

2 Methods

2.1 DFL viscoacoustic wave equation

The DFL viscoacoustic wave equation (Zhu & Harris, 2014) is defined as

$$\frac{1}{v^2} \frac{\partial^2 p}{\partial t^2} = \eta(-\nabla^2)^{1+\gamma} p + \tau \frac{\partial}{\partial t} (-\nabla^2)^{1/2+\gamma} p, \quad (1)$$

in which

$$\begin{cases} \eta = -v_0^{2\gamma} \omega_0^{-2\gamma} \cos(\pi\gamma), \tau = -v_0^{2\gamma-1} \omega_0^{-2\gamma} \sin(\pi\gamma) \\ v = v_0 \cos(\pi\gamma/2), \gamma = \arctan(1/Q)/\pi \end{cases}, \quad (2)$$

where $p = p(\mathbf{x}, t)$ represents P-wave wavefield varying in 3-D space ($\mathbf{x} = (x, y, z)$) and time (t), $\nabla^2 = \frac{\partial^2}{\partial x^2} + \frac{\partial^2}{\partial y^2} + \frac{\partial^2}{\partial z^2}$ represents the Laplacian operator in \mathbf{x} , and v_0 represents the reference velocity corresponding to the reference angular frequency ω_0 . The reference velocity and Q models can be heterogeneous in space, whereas ω_0 is fixed for the whole model.

Equation 1 can be solved by two-step extrapolation scheme (e.g., Chen et al., 2014), where 2nd-order FDs are applied for time derivatives, and pseudospectral methods for DFLs. The recursion equation is

$$p(\mathbf{x}, t + \Delta t) = \Delta t^2 v^2(\mathbf{x}) \left\{ \begin{array}{l} \eta(\mathbf{x}) \int \mathbf{W}_d(k, \mathbf{x}) \hat{p}(\mathbf{k}, t) \exp(i\mathbf{k}\mathbf{x}) d\mathbf{k} + \\ \tau(\mathbf{x}) \int \mathbf{W}_l(k, \mathbf{x}) (\hat{p}(\mathbf{k}, t) - \hat{p}(\mathbf{k}, t - \Delta t)) \exp(i\mathbf{k}\mathbf{x}) d\mathbf{k} \end{array} \right\} + 2p(\mathbf{x}, t) - p(\mathbf{x}, t - \Delta t), \quad (3)$$

in which

$$\mathbf{W}_d(k, \mathbf{x}) = k^{2\gamma(\mathbf{x})+2}, \quad (4)$$

$$\mathbf{W}_l(k, \mathbf{x}) = k^{2\gamma(\mathbf{x})+1}, \quad (5)$$

$$\hat{p}(\mathbf{k}, t) = \int p(\mathbf{x}, t) \exp(-i\mathbf{k}\mathbf{x}) d\mathbf{x}, \quad (6)$$

where i represents the imaginary unit, Δt represents the temporal step size, $\mathbf{k} = (k_x, k_y, k_z)$ represents the wavenumber vector, $k = (k_x^2 + k_y^2 + k_z^2)^{1/2}$ represents the norm of \mathbf{k} , and $\hat{p}(\mathbf{k}, t)$ represents the 3-D Fourier transform of $p(\mathbf{x}, t)$. \mathbf{W}_d and \mathbf{W}_l are mixed \mathbf{k} - \mathbf{x} domain operators, which are applied efficiently through low-rank approximation (Fomel et al., 2013).

Furthermore, to compensate for the time-stepping error caused by the 2nd-order FDs in Equation 3, an efficient strategy revises the mixed-domain operators in equations 4 and 5 as follows:

$$\mathbf{W}_d(k, \mathbf{x}) = \phi_d k^{2\gamma(\mathbf{x})+2}, \quad (7)$$

$$\mathbf{W}_l(k, \mathbf{x}) = \phi_l k^{2\gamma(\mathbf{x})+1}, \quad (8)$$

where ϕ_d and ϕ_l represent the compensators for the time-stepping errors of dispersion and loss terms, respectively. Here, we simplify the time-stepping-error compensators proposed by N. Wang et al. (2020) as follows:

$$\phi_d = \text{sinc}^{2\gamma+2}(v_0(\mathbf{x}) \Delta t k / 2), \quad (9)$$

$$\phi_l = \text{sinc}^{2\gamma+1}(v_0(\mathbf{x}) \Delta t k / 2). \quad (10)$$

160 The simplified compensators exhibit almost identical accuracy and stability to the original
 161 compensators, but are more efficient to compute during low-rank decomposition. The
 162 compensated \mathbf{W}_d and \mathbf{W}_l in equations 7 and 8 are still mixed-domain operators, which
 163 require the same number of FFTs as the uncompensated case with the same ranks.

164 At each modeling time step, the computational cost of DFLs is dominated by two
 165 forward 3-D FFTs and $(n+m)$ inverse 3-D FFTs, where n and m are the ranks along
 166 \mathbf{x} and \mathbf{k} axes for low-rank decomposition. They are integers typically between 2 and 4.
 167 In our package, we use the CuPy library for its simple python interface between the Numpy
 168 library and CUDA programming on GPU.

169 2.2 Natural-attenuation absorbing boundary conditions

170 Using CuPy library, the FFTs and elementwise operations on the entire 3-D wave-
 171 field are well organized to make full use of the GPU architecture. However, conventional
 172 ABCs require special treatments particularly on the absorbing layers, which cause dis-
 173 proportionately long runtime due to high latency from uncoalesced memory accesses in
 174 GPU. In view of this issue, we develop the naABCs, which avoid any special treatments
 175 for the absorbing layers during time marching process. The naABCs attenuate the out-
 176 going waves naturally by padding the v_0 and Q models with optimized absorbing lay-
 177 ers.

178 Considering outgoing waves at normal incidence, the returning wave amplitude from
 179 the i th absorbing layer is

$$180 A_i(\omega) = R_i(\omega) \prod_{j=0}^{i-1} (1 - R_j^2(\omega)) \exp\left(-\frac{\pi}{2}\omega \sum_{j=0}^i \Psi_j(\omega)\right), \quad i = 0, 1, \dots, N, \quad (11)$$

181 in which

$$182 R_i(\omega) = \begin{cases} \frac{|v_d^{i+1}(\omega) - v_d^i(\omega)|}{v_d^{i+1}(\omega) + v_d^i(\omega)}, & i \neq N \\ 1, & i = N \end{cases}, \quad (12)$$

$$183 \Psi_i(\omega) = 2h\gamma_a^i/v_d^i(\omega), \quad (13)$$

$$184 185 v_d^i(\omega) = v_a^i \cos(\pi\gamma_a^i/2)(\omega/\omega_0)^{\gamma_a^i}, \quad (14)$$

186 where N represents the total number of extended absorbing layers, γ_a^i and v_a^i represent
 187 model parameters at the i th layer, v_d^i represents the dispersive velocity at the i th layer,
 188 R_i represents the reflectivity between the $(i+1)$ th layer and the i th layer, and Ψ_i rep-
 189 presents the two-way attenuated traveltime (Cavalca et al., 2011) within the i th layer. Fig-
 190 ure 1 shows an illustration of the absorbing boundary, the parameters, and the proper-
 191 ties of each layer.

192 The returning wave amplitude A_i considers the primary reflection, transmission and
 193 attenuation for each sampled frequency ω within the frequency range of the source wavelet.
 194 Given the boundary parameters $\gamma_a^0 = \gamma_b$ and $v_a^0 = v_b$, we define a constrained opti-
 195 mization to solve for the minimum N and (v_a, γ_a) for each layer:

$$196 \arg \min_{(v_a^i, \gamma_a^i)} N, \quad i = 1, 2, \dots, N \quad (15)$$

$$197 \text{s.t. } A_{i-1}(\omega) \leq \epsilon_i, \quad (16)$$

$$198 \text{s.t. } \frac{\omega d}{v_d^i(\omega)} \leq \pi, \quad (17)$$

$$199 200 \text{s.t. } \frac{v_a^i \Delta t}{h} \leq s(\gamma_a^i), \quad (18)$$

201 where h is the grid size. Inequation 16 requires that the returning wave amplitude from
 202 the $(i-1)$ th absorbing layer must be smaller than the corresponding tolerance, denoted

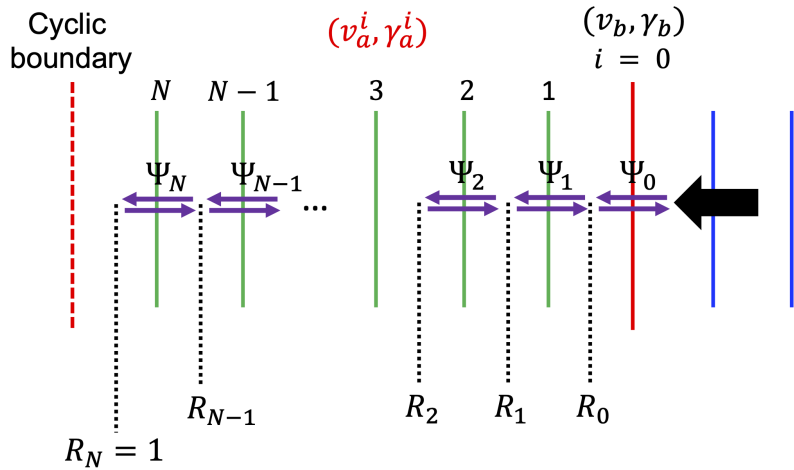


Figure 1. Illustration of natural-attenuation ABCs. The blue lines indicate the inner area, red line the model boundary, and green lines absorbing layers. The dashed red line represents the numerical cyclic boundary automatically imposed by FFTs. v_a^i and γ_a^i represent the model parameters for the i th absorbing layer, whereas v_b and γ_b represent boundary parameters. i ranges from 0 to N , which is the total number of extended absorbing layers. $i = 0$ represents the model boundary layer, thus, $v_a^0 = v_b$ and $\gamma_a^0 = \gamma_b$. R_0 to R_N represent reflectivities from the boundary layer to the outermost absorbing layer, and Ψ_0 to Ψ_N represent the two-way attenuated travel-time from the boundary layer to the outermost absorbing layer. Technically, R_N should be 0 due to the cyclic boundary. However, we can reasonably assume similar situation in the absorbing layers of the opposite boundary, so that R_N is effectively 1 for simplicity.

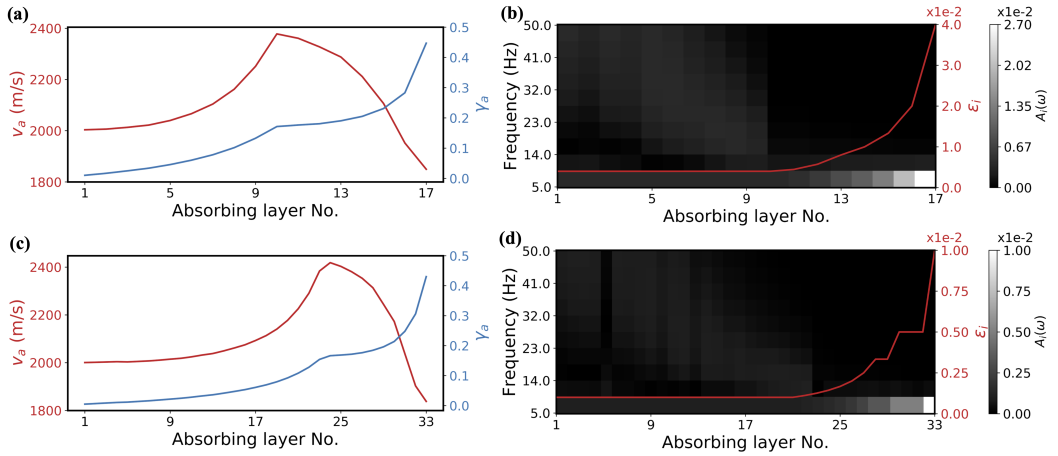


Figure 2. The optimized (v_a, γ_a) for naABCs and their corresponding returning wave amplitude for each sampled frequency from each absorbing layer. (a) and (b) are obtained when $\varepsilon = 0.04$; (c) and (d) are obtained when $\varepsilon = 0.01$.

as ϵ_i . Inequation 17 requires that all modeled wavenumber must be smaller than the Nyquist wavenumber. Inequation 18 requires that each layer's model parameters must satisfy the stability condition, given fixed ω_0 and h (see Appendix A for details about the stability condition). In Appendix B, we provide an efficient algorithm to solve this constrained optimization problem.

To test the naABCs analytically, we assume modelling parameters as $\omega_0 = 20$ Hz, $h = 20$ m, $\Delta t = 2$ ms, and model boundary parameters as $\gamma_b = 3.183 \times 10^{-3}$ (corresponding to $Q = 100$) and $v_b = 2000$ m/s. The modeling frequency ranges from 5 Hz to 50 Hz. We set the maximum A_i tolerance as $\varepsilon = 0.04$ and 0.01 for two tests, respectively (see Appendix B for details about ε and its corresponding ϵ_i).

When $\varepsilon = 0.04$, the minimum number of absorbing layers is 17, and the optimized (v_a, γ_a) are displayed in Figure 2(a). From the first absorbing layer to the outermost absorbing layer, γ_a increases monotonically, whereas v_a first increases, then decreases. The turning point for v_a variation at layer 10 is caused by the intervention of the stability condition in inequation 18.

In Figure 2(b), we show the returning wave amplitude in gray scale from each absorbing layer for each sampled frequency based on equation 11. Returning wave amplitude at all frequencies is effectively absorbed. The red line shows the amplitude tolerance varying with the layer index. The tolerance is gradually increasing from $\epsilon_1 = 0.004$ to $\epsilon_N = \varepsilon = 0.04$. Since the remaining unabsorbed frequencies become fewer as the outgoing waves propagate deeper into the absorbing layers, the maximum returning wave amplitude ϵ_i should be relaxed to avoid excessive layers just for ideal suppression of a single frequency.

If better absorption is required, we can decrease the maximum tolerance ε . Figure 2(c) shows the optimized (v_a, γ_a) when $\varepsilon = 0.01$. Now the minimum number of absorbing layers is 33. The variations of v_a and γ_a are similar to those shown in Figure 2(a), although slightly smoother. Figure 2(d) shows the returning wave amplitude and the tolerance varying along the layer index. Both of them are much smaller than those in the previous test when $\varepsilon = 0.04$.

Table 1. Model discretizations and acquisition configurations

	Homogeneous model	Heterogeneous model
Model grids ($x \times y \times z$)	$81 \times 301 \times 81$	$601 \times 301 \times 187$
Grid size (m)	20	15
Total recording time (s)	2	2
Time sampling rate (ms)	2	1
Reference frequency (Hz)	20	20
Total sources	1	1
Total receivers	4	251×51
Source location (m)	$x = 800, y = 2000, z = 800$ $x = 800$	$x = 4500, y = 2250, z = 150$ $x = \{750 + 30i i = 0, 1, \dots, 250\}$
Receiver locations (m)	$y = \{2000, 2360, 2940, 4980\}$ $z = 100$	$y = \{750 + 60i i = 0, 1, \dots, 50\}$ $z = 75$

When applying the naABCs to heterogeneous media with predetermined ε , we need to solve for N and the corresponding (v_a, γ_a) for each unique (v_b, γ_b) pair beyond the resolution limit of ($\Delta v_b = 1$ m/s, $\Delta \gamma_b = 1e - 5$). When the optimal number of absorbing layers is different for different parts of the model, we choose the maximum layer number, and extend the inner absorbing layers by repeating (v_b, γ_b) . It effectively push the boundary outward for the parts with fewer absorbing layers so that the entire model has a consistent outermost absorbing layer in view of its $A_i(\omega)$ tolerance ε .

Now we can achieve satisfying boundary absorption by directly simulating the viscoacoustic wave propagation using the padded v_0 and γ models with existing simulation codes for any computer infrastructure. Such an implementation avoids any extra partial slicing and computations specifically for the absorbing layers. The efficiency improvement by the streamlined computation is particularly significant for GPU implementations by avoiding additional delicate domain decomposition and frequent swapping of data in and out of the limited GPU memory.

3 Modeling examples

We use two modeling examples to demonstrate the effectiveness and efficiency of our modeling package with the application of naABCs. The first example is homogeneous with $v_0 = 2000$ m/s and $Q = 100$. The second example is heterogeneous, of which the velocity model is the truncated Overthrust model (Aminzadeh et al., 1997), and the Q model is derived from the velocity model by $Q = 3.516(v_0/1000)^{2.2}$ (Li, 1993). The model discretizations and acquisition configurations for these two examples are shown in Table 1. The ranks along both \mathbf{x} and \mathbf{k} for the low-rank decomposition are 2 in the homogeneous example, and 4 in the heterogeneous example. In both examples, we benchmark the absorbing effect and modeling efficiency of naABCs with the hABCs, whose acoustic application with GPU acceleration have been reported (Xie et al., 2020). The number of absorbing layers for hABCs is 20 as suggested by Liu and Sen (2018). All computations are performed on a single TITAN RTX GPU card with memory of 24GB.

3.1 Homogeneous example

We set up the homogeneous model to evaluate the absorbing effect on waves with different incident angles. The four source-receiver pairs provide four different incident angles at approximately 0° , 25° , 50° and 75° . The modeling parameters in this example are the ones used in the analytical tests for the naABCs. Hence, we pad the homoge-

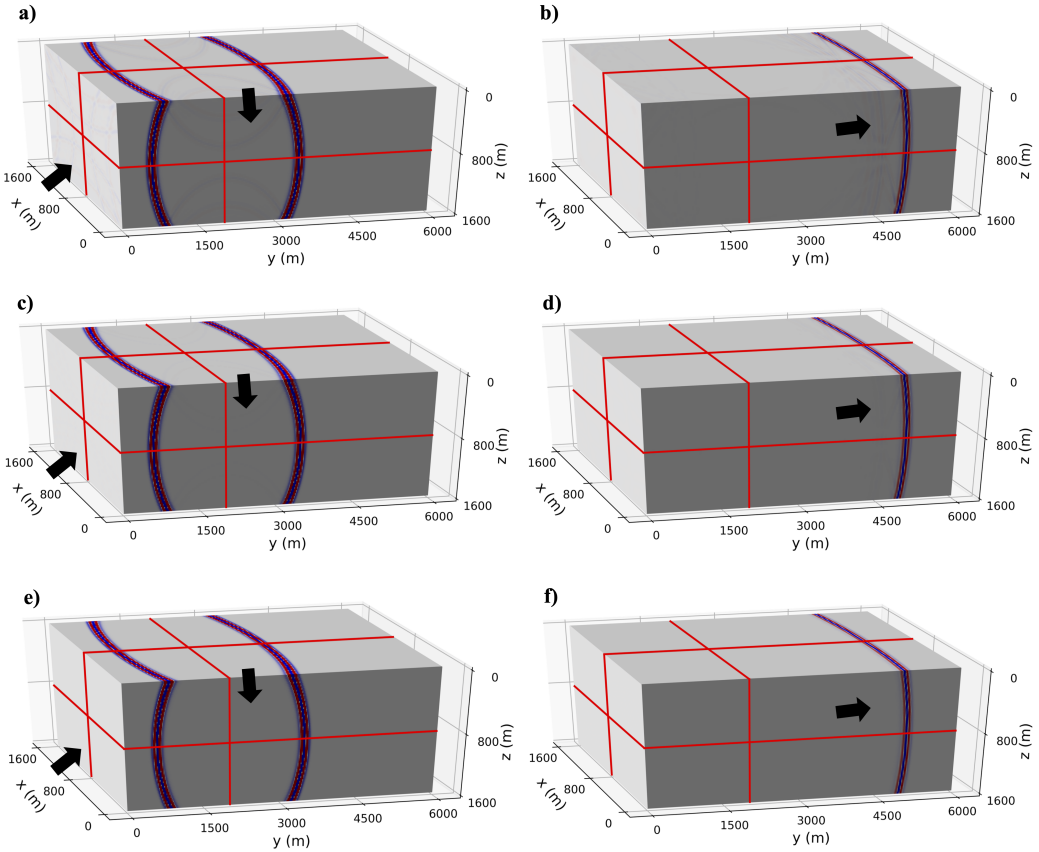


Figure 3. Snapshots at 800 ms (left column) and 1600 ms (right column) modeled using naABCs with $N = 17$ ($\varepsilon = 0.04$) (a and b), naABCs with $N = 33$ ($\varepsilon = 0.01$) (c and d), and hABCs with $N = 20$ (e and f). The red lines represent the slice positions in the 3-D wavefield volume. The black arrows indicate the potential positions of artifacts on the snapshots.

neous velocity and Q models according to the optimized (v_a, γ_a) in Figures 2(a) and 2(c), respectively. The source function is the 2nd-order derivative of a Ricker wavelet with dominant frequency as 15 Hz.

In Figure 3, we show the snapshots at 800 and 1600 ms when using naABCs and hABCs, respectively. For naABCs with $N = 17$ ($\varepsilon = 0.04$), there are weak, yet visible boundary reflections and wraparounds (see Figures 3(a) and 3(b)). For naABCs with $N = 33$ ($\varepsilon = 0.01$) and hABCs with $N = 20$ (see Figures 3(c), 3(d), 3(e), and 3(f)), we barely see any boundary artifacts in the snapshots, demonstrating excellent absorbing effect.

Figure 4 shows the recorded waveforms in comparison with the references, which are obtained by modeling with the same parameters, however, in a much larger model space with the implicit periodic boundary conditions. The hABCs show the smallest differences with the references at all tested incident angles, where the returning wave amplitude are down to 0.1% of the incident waves. Although inferior to hABCs in terms of absorbing effect, naABCs still exhibit significant absorption. Especially when $N = 33$ ($\varepsilon = 0.01$), naABCs also achieve around 0.1% boundary artifacts for relatively small

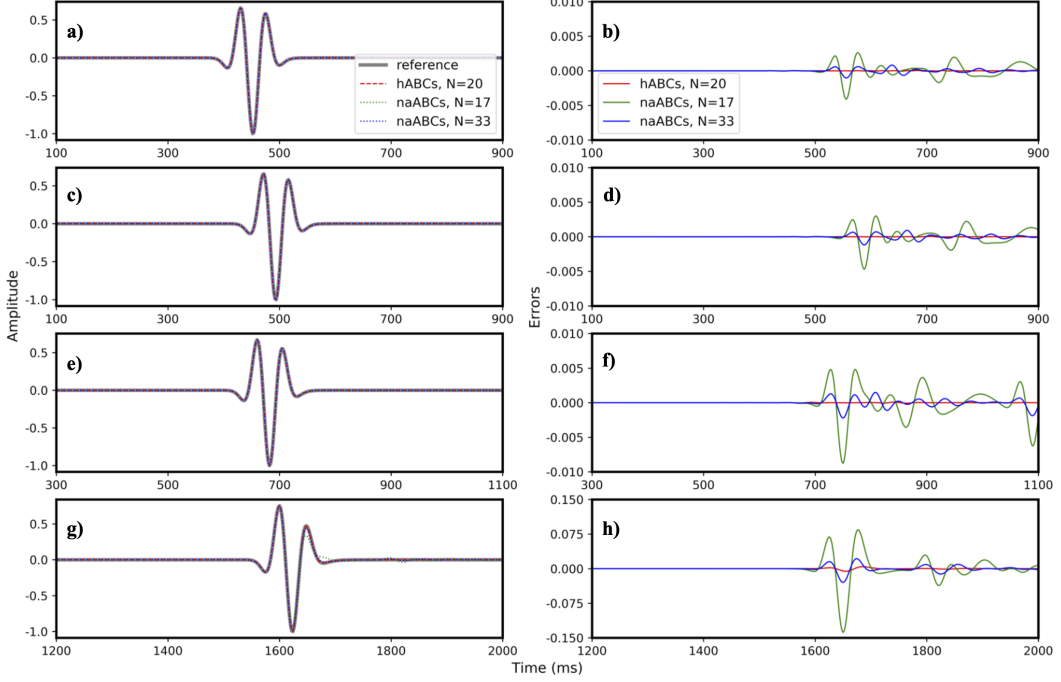


Figure 4. Comparison between normalized references and recorded waveforms modeled using naABCs and hABCs. The four rows correspond to the incident angles of 0° (a and b), 25° (c and d), 50° (e and f), and 75° (g and h). The left column displays the normalized references and modeled waveforms, while the right column shows their differences.

Table 2. Runtime of different procedures for 3-D viscoacoustic modeling with different ABCs in the homogeneous model.

Runtime (s) \ ABCs	naABCs ($\varepsilon = 0.04$) $N = 17$	naABCs ($\varepsilon = 0.01$) $N = 33$	hABCs $N = 20$
Procedure			
ABCs preparation	6.55	9.10	1.53
Low-rank decomposition	1.20	1.89	1.18
Modeling (1000 time steps)	9.14	18.98	58.76
Total	16.89	29.97	61.47

and moderate incident angles as 0° , 25° , and 50° (see Figures 4(b), 4(d), and 4(f)), whereas around 1% for incident angle as large as 75° (see Figure 4(h)).

Table 2 shows the runtime of different procedures when modeling with different ABCs. The preparation time for naABCs is longer, due to the extra parameter optimization for the absorbing layers. For low-rank decomposition, the computational cost is dominated by composing submatrices of the mixed-domain operators shown in equations 7 and 8. Thus, more absorbing layers in naABCs ($\varepsilon = 0.01$) lead to slightly increasing runtime. Compared to hABCs with $N = 20$, the time marching process, which contributes most to the runtime, shows approximately 6x and 3x speedup when using naABCs with $N = 17$ and $N = 33$, respectively. Therefore, the overall modeling time with naABCs can achieve at least 2x speedup over hABCs.

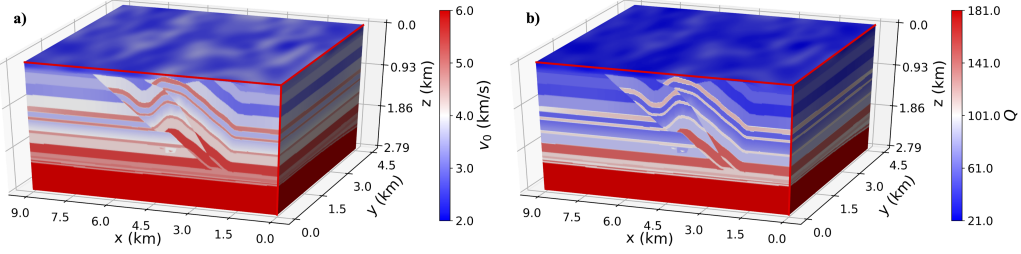


Figure 5. (a) Truncated Overthrust velocity model and its corresponding (b) Q model.

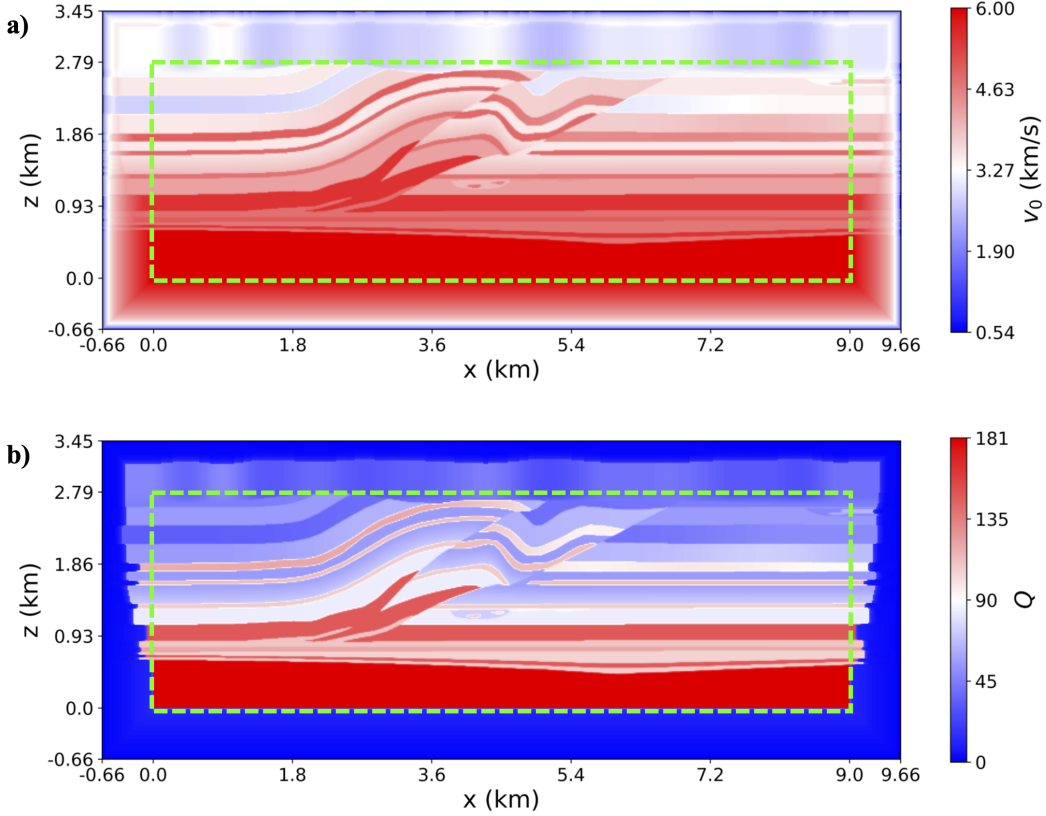


Figure 6. Padded (a) Velocity and (b) Q model slices at $y = 2000$ m for naABCs ($\varepsilon = 0.05$). The green dashed box delineates the original model area.

291

3.2 Heterogeneous example

292

We employ the models shown in Figure 5 to evaluate the accuracy and efficiency
293 of our modeling package for complex heterogeneous model. The source function here is
294 the 2nd-order derivative of a Ricker wavelet with dominant frequency of 20 Hz. Corre-
295 spondingly, the frequency for naABCs optimization ranges from 8 Hz to 62 Hz. There
296 are total 1708 unique pairs of (v_b, γ_b) . We use $\varepsilon = 0.05$, resulting in maximum num-
297 ber of absorbing layers as 44. Figure 6 displays the padded velocity and Q model slices
298 at $y = 2000$ m for naABCs. The padded absorbing layers show much smaller velocity
299 and Q in order to attenuate the outgoing waves naturally.

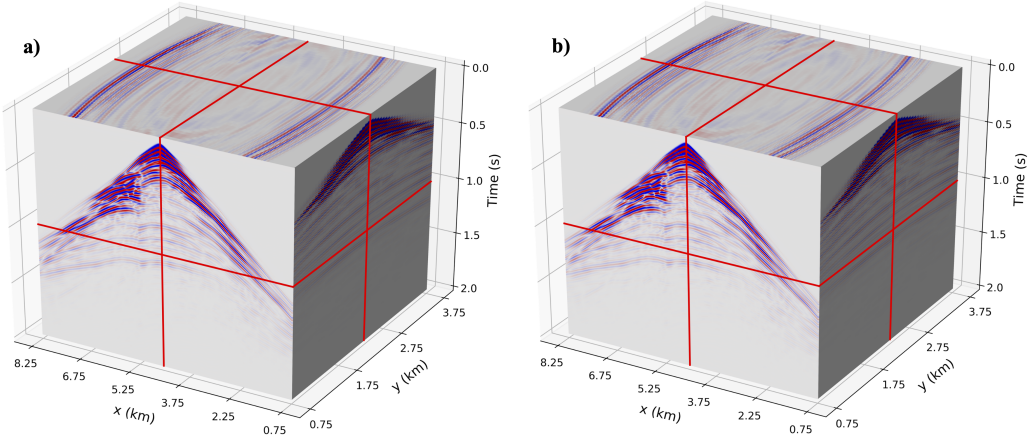


Figure 7. Modeled 3-D seismic data volume using (a) hABCs with $N = 20$, and (b) naABCs with $N = 44$ ($\varepsilon = 0.05$). The red lines indicate the slice positions for displaying the 3-D data volume.

Table 3. Runtime of different procedures for 3-D viscoacoustic modeling with different ABCs in the heterogeneous model.

Procedure \ ABCs	naABCs ($\varepsilon = 0.05$) $N = 44$	hABCs $N = 20$
ABCs preparation	125.72	8.01
Low-rank decomposition	38.33	25.35
Modeling (2000 time steps)	469.31	995.56
Total	633.36	1028.92

Figure 7 displays the modeled 3-D seismic data volume using our modeling package with naABCs and hABCs, respectively. The two modeled seismograms are consistent with each other without any visible artifacts. We show two specific traces with near (670 m) and far (3795 m) offsets, respectively, in Figure 8. The waveforms from naABCs (blue dashed lines) agree reasonably well with those from hABCs (red lines).

Table 3 shows the runtime of different procedures when applying different ABCs in this modeling example. The runtime for all procedures increases significantly due to larger model dimension, more modeling time steps, and the heterogeneity of velocity and Q models. The preparation time for naABCs here is much longer than hABCs, due to the parameter optimizations for more unique pairs of (v_b, γ_b) in the heterogeneous case. Cost for low-rank decomposition in naABCs is reasonably larger than that in hABCs caused by the difference between their numbers of absorbing layers. The iterative modeling process when applying naABCs is more than 2x faster than applying hABCs. Furthermore, with increasing number of shots and modeling time steps, the computational cost for ABCs preparation and low-rank decomposition will become less considerable and eventually negligible. Hence, our modeling package using naABCs in heterogeneous case can achieve around 2x speedup over conventional hABCs.

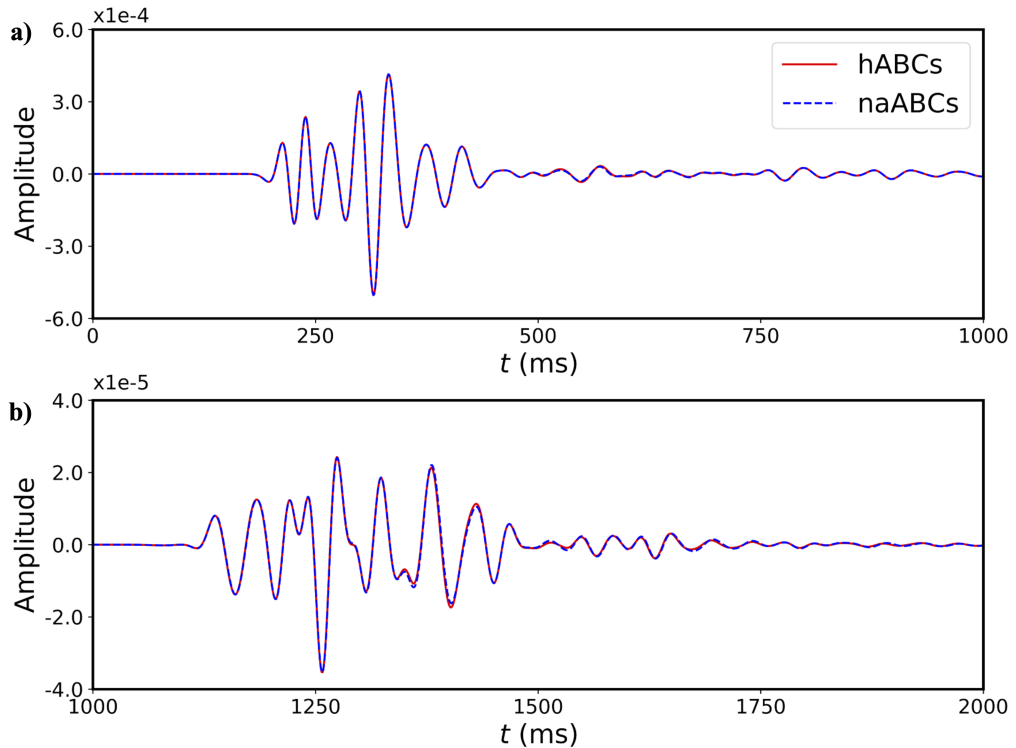


Figure 8. Modeled trace comparison using hABCs with $N = 20$ and naABCs with $N = 44$ ($\varepsilon = 0.05$). The two traces are recorded from receivers at (a) ($x = 4800$ m, $y = 2850$ m) and (b) ($x = 900$ m, $y = 1050$ m), respectively.

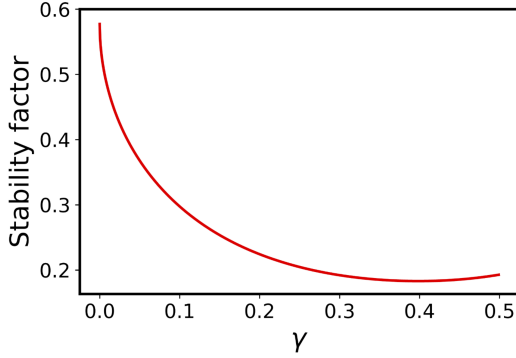


Figure A1. Stability factor varying with γ within $[0, 0.5]$ when $\omega_0 = 20 \times 2\pi$ and $h = 20$ m.

4 Conclusion

We develop a python package for GPU-accelerated 3-D P-wave simulation in anelastic media based on the DFL viscoacoustic wave equation. The package utilizes two-step extrapolation with simplified time-stepping error compensation. The proposed naABCs based on optimized absorbing layer parameters, naturally attenuate the boundary artifacts. Modeling examples demonstrate that the naABCs provide approximately 2x speedup over the conventional hABCs with satisfying simulation accuracy.

Appendix A Stability condition

Let $p^{-1} = p(\mathbf{x}, t - \Delta t)$, $p^0 = p(\mathbf{x}, t)$, and $p^1 = p(\mathbf{x}, t + \Delta t)$ represent the wavefields at three consecutive time steps, an abbreviated matrix notation for the recursion equation 3 is

$$\begin{bmatrix} p^1 \\ p^0 \end{bmatrix} = \begin{bmatrix} g_1 & g_0 \\ 1 & 0 \end{bmatrix} \begin{bmatrix} p^0 \\ p^{-1} \end{bmatrix}, \quad (\text{A1})$$

in which

$$g_0 = r/h \sin(\pi\gamma) \cos(\pi\gamma/2)^2 \omega_0^{-2\gamma} \mathbf{W}_l - 1, \quad (\text{A2})$$

$$g_1 = -r^2/h^2 \cos(\pi\gamma) \cos^2(\pi\gamma/2) \omega_0^{-2\gamma} \mathbf{W}_d - g_0 + 1, \quad (\text{A3})$$

where $r = v_0 \Delta t / h$ represents the Courant number.

According to the eigenvalue method (Gazdag, 1981), the recursion is stable only if the eigenvalues of the transition matrix in equation A1 are less or equal to 1. Hence, we have the stability condition as

$$-1 \leq g_0 \leq 1 - |g_1|. \quad (\text{A4})$$

Knowing ω_0 , h , and γ , we can search for the largest r satisfying inequation A4 with $kh = \sqrt{3}\pi$, i.e., $k_x h = k_y h = k_z h = \pi$ in 3-D case. This largest r is the stability factor $s(\gamma)|_{(\omega_0, h)}$ utilized in the inequation 18. Figure A1 shows the stability factor varying with γ when $\omega_0 = 20 \times 2\pi$ and $h = 20$ m. As γ increases, $s(\gamma)$ decreases, indicating harsher stability condition. Prior to the parameter optimization for naABCs, we search for stability factors of regularly sampled γ within $[0, 0.5]$. So during the optimization, the stability factor for any tested γ is readily obtained by nearest interpolation of the predetermined stability factor samples.

346 Appendix B Optimization for naABCs

347 The constrained optimization in 15 is a trans-dimensional inversion problem, which
 348 can be solved by Bayesian inversion based on reversible jump Markov-chain Monte Carlo
 349 (MCMC) sampling (Sambridge et al., 2006). However, for each unique (v_b, γ_b) pair, it
 350 requires to solve several fixed dimension inversion problems with different N , resulting
 351 in tremendous computational cost in the heterogeneous case. Additionally, it is difficult
 352 to determine the viable lower bounds of N for different (v_b, γ_b) , since the sampled N could
 353 be too small to have a solution of (v_a, γ_a) satisfying all constraints in inequations 16, 17,
 354 and 18.

355 Noticing the three constraints require no information beyond the i th layer, we re-
 356 place the trans-dimensional inversion by a sequential optimization. At each step, it solves
 357 for the two model parameters of the current i th layer (v_a^i, γ_a^i) , until all constraints are
 358 satisfied with $R_i = 1$, indicating $i = N$ according to equation 12.

359 For the i th layer, model parameters of the inner layers is either initialized or al-
 360 ready solved. Now to achieve the minimum N , we should maximize the attenuation within
 361 the i th layer:

$$362 \arg \min_{(v_a^i, \gamma_a^i)} \max \left\{ \exp \left(-\frac{\pi}{2} \omega \Psi_i(\omega) \right) \mid \omega \in \omega_s^i \right\}, \quad (B1)$$

363 where $\omega_s^i = [\omega_0, \omega_1, \omega_2, \dots, \omega_I]^T$ represents the angular frequency samples that are not
 364 being absorbed yet. Initially, ω_s^0 is regularly sampled from the modeled frequency range.
 365 The number of initial samples is empirically set as 10 for a balance of accuracy and ef-
 366 ficiency.

367 As i increases, higher frequencies will satisfy inequation 16 with $R_i = 1$ first, re-
 368 sulting in a smaller set of unabsorbed frequency samples as follows:

$$369 \omega_s^i = \{ \omega \mid \alpha_{i-1}(\omega) > \epsilon_{i-1}, \omega \in \omega_s^{i-1} \}. \quad (B2)$$

370 in which

$$371 \alpha_i(\omega) = A_i(\omega) \mid R_i = 1. \quad (B3)$$

372 With fewer frequency samples in ω_s^i , the tolerance for the maximum returning wave am-
 373 plitude should be relaxed as follows:

$$374 \epsilon_i = \varepsilon / I, \quad (B4)$$

375 where ε represents the maximum tolerance for the outermost layer, I represents the num-
 376 ber of samples in ω_s^i . Hence, $\epsilon_0 = \varepsilon / 10$ and $\epsilon_N = \varepsilon$. Although ϵ_i can also be constant
 377 for simplicity, we find that this increasing ϵ_i generally provides satisfying absorption with
 378 smaller N .

379 Now we are solving a fixed dimensional constrained optimization with minimax ob-
 380 jective B1 and inequations constraints 16, 17, and 18, for the current i th layer. Such a
 381 problem can be solved efficiently by grid search combined with linear programming. Given
 382 a tentative γ_a^i , inequation 16 provides both a lower bound $v_l^{(1)}$ and an upper bound $v_u^{(1)}$
 383 for v_a^i as follows:

$$384 v_l^{(1)} = \max \left\{ \frac{1 - \epsilon_i / \alpha_{i-1}(\omega)}{1 + \epsilon_i / \alpha_{i-1}(\omega)} \frac{v_d^{i-1}(\omega)}{\beta_i(\omega)} \mid \omega \in \omega_s^i \right\} \quad (B5)$$

$$385 v_u^{(1)} = \min \left\{ \frac{1 + \epsilon_i / \alpha_{i-1}(\omega)}{1 - \epsilon_i / \alpha_{i-1}(\omega)} \frac{v_d^{i-1}(\omega)}{\beta_i(\omega)} \mid \omega \in \omega_s^i \right\}, \quad (B6)$$

387 in which

$$388 389 \beta_i(\omega) = \cos(\pi \gamma_a^i / 2) (\omega / \omega_0)^{\gamma_a^i}. \quad (B7)$$

390 Inequations 17 and 18 provide another lower bound $v_l^{(2)}$ and another upper bound $v_u^{(2)}$,
 391 respectively, for v_a^i as follows:

$$392 \quad v_l^{(2)} = \max\left\{\frac{\omega h}{\pi\beta_i(\omega)} \mid \omega \in \omega_s^i\right\}, \quad (B8)$$

$$393 \quad v_u^{(2)} = \frac{s(\gamma_a^i)h}{\Delta t}. \quad (B9)$$

395 For this γ_a^i , the smallest v_a^i satisfying all bounds in equations B5, B6, B8, and B9 will
 396 provide the maximum attenuation. Thus, as the outer loop being the grid search for γ_a^i ,
 397 and inner loop being the linear programming for v_a^i , we can solve for the optimal (v_a^i, γ_a^i)
 398 for the minimax objective B1. Note that there always be at least one viable solution of
 399 (v_a^i, γ_a^i) for this constrained optimization, that is $(v_a^{i-1}, \gamma_a^{i-1})$.

400 As i increasing, the remaining unabsorbed frequency samples become fewer. Eventually,
 401 all frequency samples will satisfy the constraints with $R_i = 1$, causing $I = n(\omega_s^i) =$
 402 0. Then, we stop the sequential optimization and obtain the minimum $N = i$ with cor-
 403 responding (v_a, γ_a) . We summarize the workflow of parameter optimization for naABCs
 404 in Algorithm 1.

405 Acknowledgments

406 Enter acknowledgments, including your data availability statement, here.

407 References

- 408 Aminzadeh, F., Jean, B., & Kunz, T. (1997). *3-d salt and overthrust models*. Society
 409 of Exploration Geophysicists.
- 410 Berenger, J.-P., et al. (1994). A perfectly matched layer for the absorption of elec-
 411 tromagnetic waves.
- 412 Carcione, J. M., Cavallini, F., Mainardi, F., & Hanyga, A. (2002). Time-domain
 413 modeling of constant-q seismic waves using fractional derivatives. *Pure and
 414 Applied Geophysics*, 159(7-8), 1719–1736.
- 415 Cavalca, M., Moore, I., Zhang, L., Ng, S. L., Fletcher, R., & Bayly, M. (2011). Ray-
 416 based tomography for Q estimation and Q compensation in complex media. In
 417 *81st annual international meeting, seg, extended abstracts* (pp. 3989–3993).
- 418 Chen, H., Zhou, H., Jiang, S., & Rao, Y. (2019). Fractional laplacian viscoacoustic
 419 wave equation low-rank temporal extrapolation. *Ieee Access*, 7, 93187–93197.
- 420 Chen, H., Zhou, H., Li, Q., & Wang, Y. (2016). Two efficient modeling schemes
 421 for fractional laplacian viscoacoustic wave equation. *Geophysics*, 81(5), T233–
 422 T249.
- 423 Chen, H., Zhou, H., & Qu, S. (2014). Lowrank approximation for time domain vis-
 424 coacoustic wave equation with spatially varying order fractional laplacians. In
 425 *Seg technical program expanded abstracts 2014* (pp. 3400–3405). Society of Ex-
 426 ploration Geophysicists.
- 427 Dutta, G., & Schuster, G. T. (2014). Attenuation compensation for least-squares re-
 428 verse time migration using the viscoacoustic-wave equation. *Geophysics*, 79(6),
 429 S251–S262.
- 430 Fomel, S., Ying, L., & Song, X. (2013). Seismic wave extrapolation using lowrank
 431 symbol approximation. *Geophysical Prospecting*, 61, 526–536.
- 432 Gazdag, J. (1981). Modeling of the acoustic wave equation with transform methods.
 433 *Geophysics*, 46(6), 854–859.
- 434 Kjartansson, E. (1979). Constant Q -wave propagation and attenuation. *Journal of
 435 Geophysical Research: Solid Earth*, 84(B9), 4737–4748.
- 436 Li, Q. Z. (1993). *High-resolution seismic exploration*. Petroleum Industry Press.
- 437 Liu, Y., & Sen, M. K. (2010). A hybrid scheme for absorbing edge reflections in nu-
 438 matical modeling of wave propagation. *Geophysics*, 75(2), A1–A6.

Algorithm 1 Parameter optimization for naABCs**Input:**

Modeling parameters: $\omega_0, \Delta t, h$
 Model boundary parameters: v_b, γ_b
 Optimization parameters: ω_s^0, ε
 Grid search radius for γ_a : R_γ
 Grid search number for γ_a : M

Output:

minimum number of absorbing layers: N
 parameters for N absorbing layers: v_a, γ_a

Initialization:

$v_a^0 \leftarrow v_b, \gamma_a^0 \leftarrow \gamma_b$
 Compute $s(\gamma), \gamma \in [0, 0.5]$
 Compute $v_d^0(\omega), \Psi_0(\omega), \alpha_0(\omega), \omega \in \omega_s^0$
 $I \leftarrow n(\omega_s^0)$
 $\epsilon_0 \leftarrow \varepsilon/I$
 $i \leftarrow 0$

Iteration:

```

while  $I > 0$  do
     $i++$ 
    Update  $\omega_s^i, I, \epsilon_i$ 
     $\gamma_l \leftarrow \max(\gamma_a^{i-1} - R_\gamma, 0)$ 
     $\gamma_u \leftarrow \min(\gamma_a^{i-1} + R_\gamma, 0.5)$ 
     $\Delta\gamma \leftarrow (\gamma_u - \gamma_l)/M$ 
     $J_{min} \leftarrow \infty$ 
    for  $j = 0, 1, \dots, M$  do
         $\gamma \leftarrow \gamma_l + j\Delta\gamma$ 
        Compute  $\beta_i(\omega), \omega \in \omega_s^i$ 
        Compute  $v_l^{(1)}, v_u^{(1)}, v_l^{(2)}, v_u^{(2)}$ 
         $v_l \leftarrow \max(v_l^{(1)}, v_l^{(2)})$ 
         $v_u \leftarrow \min(v_u^{(1)}, v_u^{(2)})$ 
        if  $v_l \leq v_u$  then
             $v \leftarrow v_l$ 
            Compute  $v_d^i(\omega), \omega \in \omega_s^i$ 
            Compute  $\Psi_i(\omega), \omega \in \omega_s^i$ 
             $J \leftarrow \max\{\exp(-\frac{\pi}{2}\omega\Psi_i(\omega)) | \omega \in \omega_s^i\}$ 
            if  $J < J_{min}$  then
                 $J_{min} \leftarrow J$ 
                 $\gamma_a^i \leftarrow \gamma, v_a^i \leftarrow v$ 
            end if
        end if
    end for
    Compute  $R_{i-1}(\omega), \omega \in \omega_s^i$ 
    Compute  $\alpha_i(\omega)$ 
end while
 $N \leftarrow i$ 

```

- Liu, Y., & Sen, M. K. (2018). An improved hybrid absorbing boundary condition for wave equation modeling. *Journal of Geophysics and Engineering*, 15(6), 2602–2613.
- McDonal, F., Angona, F., Mills, R., Sengbush, R., Van Nostrand, R., & White, J. (1958). Attenuation of shear and compressional waves in pierre shale. *Geophysics*, 23(3), 421–439.
- Ren, Z., & Liu, Y. (2013). A hybrid absorbing boundary condition for frequency-domain finite-difference modelling. *Journal of Geophysics and Engineering*, 10(5), 054003.
- Sambridge, M., Gallagher, K., Jackson, A., & Rickwood, P. (2006). Trans-dimensional inverse problems, model comparison and the evidence. *Geophysical Journal International*, 167(2), 528–542.
- Sanders, C., Ponko, S., Nixon, L., & Schwartz, E. (1995). Seismological evidence for magmatic and hydrothermal structure in long valley caldera from local earthquake attenuation and velocity tomography. *Journal of Geophysical Research: Solid Earth*, 100(B5), 8311–8326.
- Sun, J., Fomel, S., Zhu, T., & Hu, J. (2016). Q-compensated least-squares reverse time migration using low-rank one-step wave extrapolation. *Geophysics*, 81(4), S271–S279.
- Wang, N., Zhu, T., Zhou, H., Chen, H., Zhao, X., & Tian, Y. (2020). Fractional laplacians viscoacoustic wavefield modeling with k -space-based time-stepping error compensating scheme. *Geophysics*, 85(1), T1–T13.
- Wang, Y., Zhou, H., Zhao, X., Zhang, Q., Zhao, P., Yu, X., & Chen, Y. (2019). Cu q-rtm: A cuda-based code package for stable and efficient q-compensated reverse time migration. *Geophysics*, 84(1), F1–F15.
- Xie, C., Song, P., Tan, J., Liu, B., Li, J., Yu, K., ... Zhang, R. (2020). Cosine-type weighted hybrid absorbing boundary based on the second-order higdon boundary condition and its gpu implementation. *Journal of Geophysics and Engineering*, 17(2), 231–248.
- Xu, Y., Li, J., Pang, G., Wang, Z., Chen, X., & Wang, B. (2018). A new radial basis function collocation method based on the quasi-uniform nodes for 2d fractional wave equation. *arXiv preprint arXiv:1806.01846*.
- Xue, Z., Sun, J., Fomel, S., & Zhu, T. (2018). Accelerating full-waveform inversion with attenuation compensation. *Geophysics*, 83(1), A13–A20.
- Yao, J., Zhu, T., Hussain, F., & Kouri, D. J. (2017). Locally solving fractional laplacian viscoacoustic wave equation using hermite distributed approximating functional method. *Geophysics*, 82(2), T59–T67.
- Zhang, J., Wu, J., & Li, X. (2013). Compensation for absorption and dispersion in prestack migration: An effective q approach. *Geophysics*, 78(1), S1–S14.
- Zhu, T., Ajo-Franklin, J. B., & Daley, T. M. (2017). Spatiotemporal changes of seismic attenuation caused by injected CO₂ at the Frio-II pilot site, Dayton, TX, USA. *Journal of Geophysical Research: Solid Earth*, 122, 7156–7171.
- Zhu, T., & Harris, J. M. (2014). Modeling acoustic wave propagation in heterogeneous attenuating media using decoupled fractional laplacians. *Geophysics*, 79(3), T105–T116.
- Zhu, T., Harris, J. M., & Biondi, B. (2014). Q-compensated reverse-time migration. *Geophysics*, 79(3), S77–S87.